

## High resolution study of etch figures on CaF<sub>2</sub> (111)

Christian Motzer and Michael Reichling<sup>a)</sup>*Fachbereich Physik, Universität Osnabrück, Barbarastr. 7, 49076 Osnabrück, Germany*

(Received 9 October 2008; accepted 16 December 2008; published online 19 March 2009)

Calcium difluoride crystals cleaved along the (111) direction are etched with the dislocation site selective etchants HNO<sub>3</sub>, HCl, H<sub>2</sub>SO<sub>4</sub>, and H<sub>3</sub>PO<sub>4</sub> and their surfaces are inspected *ex situ* with scanning force microscopy (AFM). Force microscopy yields characteristic features of the etch pits at the nanometer scale such as terracing and ditrigonal patterns. The method enables direct quantitative measurements of etch pit structures to derive kinetic data revealing details of the dissolution mechanism. Orthophosphoric acid is found to yield the best scaleable etching figures at ambient and elevated temperatures, as for this etchant, the dissolution is reaction-rate controlled. The scanning tip can induce a precipitationlike process by adherent traces of sulfuric or phosphoric acid that can be removed by a treatment with nitric acid following the regular etching procedure.

© 2009 American Institute of Physics. [DOI: [10.1063/1.3078774](https://doi.org/10.1063/1.3078774)]

### I. INTRODUCTION

Calcium difluoride (fluorite, CaF<sub>2</sub>) is one of the very few materials that is optically transparent in the deep ultraviolet (DUV) spectral region.<sup>1,2</sup> Because of its wide band gap and other exceptional material properties such as a high laser-damage threshold,<sup>3</sup> low axial and radial-stress birefringence,<sup>4</sup> and a high refractive index,<sup>4</sup> it is the first choice material for DUV optical applications. After tremendous efforts in developing large-scale growth methods, industry is now able to produce high quality synthetic fluorite as large crystals.<sup>5</sup> However, residual intrinsic crystal defects, such as dislocations causing birefringence<sup>6</sup> and extrinsic defects causing absorption,<sup>7</sup> degrade the optical quality and limit the use of CaF<sub>2</sub> as a DUV optical material.

Dislocations are one-dimensional crystal lattice defects and relicts of growth perturbations or a result from crystal handling and preparation. Their detection, characterization, and control is one of the major challenges for large-scale production of fluorite for DUV optical applications.<sup>5</sup> To fully develop and exploit the potential of the fluorite technology, the rapid development of fluorite crystal growth technology must be accompanied by the development of advanced analysis techniques allowing for a quality control with regard to bulk and surface properties. In the present work we demonstrate an approach to the analysis of etch pits on fluorite based on scanning force microscopy (SFM) (often referred to as AFM) to reveal in-depth information on dislocations and near-surface defects. Recently, etching has also gained much interest as a method for the characterization of GaN wafers<sup>8</sup> where the present work also contributes to the understanding of etching phenomena observed for this material.

The technique of etching crystal faces has originally been established as an inspection method for revealing the quality of crystals with respect to their content of dislocations. Cockayne and Robertson<sup>9</sup> demonstrated for CaF<sub>2</sub> that

site-selective etchants mark dislocations defects on the surface with etch pits that can be detected with an optical microscope. Various etching conditions suitable for marking dislocation defects were tested on natural and synthetic fluorite by Kleber *et al.*<sup>10</sup> In all of these investigations, the detection of etch figures was performed using optical or electron microscopy techniques<sup>11,12</sup> and the analysis was mostly restricted to determining the etch pit density (EPD) which is often taken as a figure of merit for the investigated crystals. However, as etching figures can be caused by different processes that cannot simply be discriminated by accounting for the EPD, this number, in fact, provides only an indicative figure for crystal quality and does not allow a detailed analysis of crystal properties.

For a classification and in-depth analysis of different defect structures, it is highly desirable to fully characterize etching figures with respect to their size, shape, and topography and to establish a relationship between a certain morphological characteristics and the type of defect creating the etching figure. SFM operated in the contact mode is a suitable technique for this as it allows us to determine the surface topography of insulating crystals with nanometer precision and, hence, a detailed analysis of etch pits. In the context of crystal dissolution studies, such analysis has so far mainly been used for the characterization of growth quality of gallium nitride wafers<sup>8</sup> and for studying dissolution kinetics of calcite.<sup>13,14</sup> For fluorite surface studies, SFM has been demonstrated to be most useful for the analysis of *in situ* crystal growth and dissolution,<sup>15</sup> surface roughness measurements,<sup>16</sup> and the highest resolution surface characterization of superpolished surfaces.<sup>17</sup>

While optical microscopy analysis is well suited to counting larger etch pits, SFM is the ideal tool for detecting small etch pits and for a detailed analysis of etch pit topography and classification into morphological categories. Considering a typical EPD of 10<sup>5</sup> cm<sup>-2</sup> on the (111) cleaved surface of synthetic CaF<sub>2</sub> crystals,<sup>9</sup> the average distance between dislocations on the surface is about 30 μm while the dislocation interspacing in small angle grain boundaries may

<sup>a)</sup> Author to whom correspondence should be addressed. Electronic mail: [reichling@uos.de](mailto:reichling@uos.de). Tel.: ++49 541 969-2264. FAX: ++49 541 969-12264.

be much smaller. As the lateral resolution power of the SFM is way beyond the micrometer regime, this technique yields excellent results not only under standard conditions but also in cases of a very high EPD. The SFM allows a detailed analysis of the depth and lateral extension of the etch pit and the detailed structure of its walls. However, SFM is also capable of characterizing much smaller etch pits than optical microscopy which is desirable in industrial quality control where high-end surfaces may be characterized during the production process and subsequent polishing efforts to remove etching figures can be limited to a minimum.

Several dislocation site-selective etches such as nitric acid ( $\text{HNO}_3$ ),<sup>18</sup> hydrochloric acid ( $\text{HCl}$ ),<sup>19</sup> sulfuric acid ( $\text{H}_2\text{SO}_4$ ),<sup>20,21</sup> and orthophosphoric acid ( $\text{H}_3\text{PO}_4$ ) (Ref. 10) have been described in literature for etching (111) cleavage plates of fluorite which all allow dislocations to be revealed. In the present study we compare the morphology of the etching figures resulting from different acids by applying *ex situ* SFM. We discuss several morphological aspects such as the terracing of etch pit walls, the occurrence of ditrigonal etch pit borders and the retarded growth of surface protrusions as well the associated dissolution kinetics. By acquiring quantitative data, we are able to distinguish between different types of etch pits and understand their origin.

## II. EXPERIMENTAL SECTION

Calciumdifluoride crystals (UV quality,  $20 \times 20 \text{ mm}^2$  cross section from Korth Kristalle GmbH Kiel, Germany) are cleaved parallel to the (111) plane using a sharp blade. For etching, each cleavage sample is held vertically with plastic tweezers in  $40 \text{ cm}^3$  of the etch solution. The etch is kept in a beaker without stirring while the temperature is kept constant by a thermostatic bath where the etching temperature can be stabilized to values between 293 and 373 K. After the desired etch duration that varies from 5 to 45 min, the sample is removed from the beaker, dipped into a sodium hydroxide solution ( $\text{pH}=8-9$ ) for 1 s to remove acid traces, then dipped into distilled water for a few seconds, and finally dried with lint-free paper and in a stream of dry nitrogen. In later experiments we used nitric acid instead of sodium hydroxide to remove precipitates from the etching process.

After this preparation, the sample is investigated with a contact-mode SFM (easyScan Nanosurf Liestal, Switzerland). The SFM control software is configured to scan areas up to  $50 \times 50 \mu\text{m}^2$  at a scan speed up to one line per second. The typical relative uncertainty in dimensional analysis of SFM images of etch pits is less than 5% as determined from measurements with calibrated test grids. Images are displayed in a derivative mode enhancing image contrast and allowing a detailed analysis of the slopes of etch pits. This derivative mode displays the negative surface slope along a horizontal line with a darker gray level and a positive surface slope with a lighter gray level.

The Arrhenius graph (Fig. 4) is derived from the data of lateral etching speed  $v_L$  measured at different temperatures  $T$ . To determine the speed  $v_L$  for a specific temperature, three different etch times  $t$  between 5 and 45 min are chosen. From each investigated sample, up to five of the largest etch pits

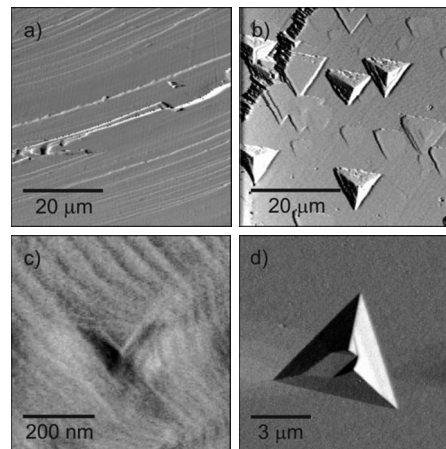


FIG. 1. (a)  $\text{CaF}_2$  surface cleaved parallel to the (111) plane exhibiting cleavage steps with a height of up to 110 nm. (b) After etching 5 min in concentrated nitric acid at 313 K, the surface is covered with etching figures, namely, pointed etch pits having a depth of up to 800 nm, flat bottom etch pits having a depth of typically 50 nm, and corroded step edges. (c) Example for imaging a small etch pit (concentrated phosphoric acid for 5 min at 353 K) with a lateral dimension of 250 nm and a depth of 20 nm. The diagonal stripes represent F-Ca-F triple-layer step edges with a height of 0.315 nm. (d) Occasionally, etch pits exhibit complex shapes like this double pointed etch pit (concentrated phosphoric acid for 20 min at 363 K).

are taken to determine the maximum edge length  $L$ . The lateral speed  $v_L$  is calculated from the edge length  $L$  via  $v_L = 1/4(L/t)$  assuming an equilateral triangle. By plotting the logarithm of the lateral step speed  $v_L$  against the reciprocal absolute temperature  $T$  the slope of the linear graph relates to the activation energy  $E = -k \partial \ln(v_L) / \partial (1/T)$ , where  $k$  is the Boltzmann constant.

## III. RESULTS AND DISCUSSION

### A. Basic observations

#### 1. Surface structure and etch pits

The surface we investigate originates from the  $\text{CaF}_2$  (111) cleavage plane exhibiting atomically flat terraces separated by cleavage steps with a height of one or multiple (F-Ca-F) triple layers (with integer multiples of 0.315 nm); a typical example is shown in Fig. 1(a). Much larger steps than triple layers are produced depending on the detailed distribution of stress in the crystal during cleavage. Small cleavage steps consisting of only a few triple layers often appear in a zigzag pattern whereas larger cleavage steps usually appear as straight or slightly curved lines.<sup>22</sup> The naturally occurring steps created by cleavage of a  $\text{CaF}_2$  (111) surface are predominantly oriented in the [110] direction.<sup>22</sup>

The treatment with acid causes the surface to retreat over the entire area and to produce specific etch figures. The characteristic features observed are the development of pointed pits (embossed pyramids) and flat bottomed pits (shallow troughs) and corrosion of cleavage steps as evident in Fig. 1(b). The size of etch pits ranges from nanometer dimensions to several  $10 \mu\text{m}$  depending on etching conditions. Our SFM has sufficient resolving power to investigate etch pits of only a few nanometer depth as demonstrated in Fig. 1(c). Occasionally we observe etch pits having a complicated structure at their bottom as seen in Fig. 1(d); further on we

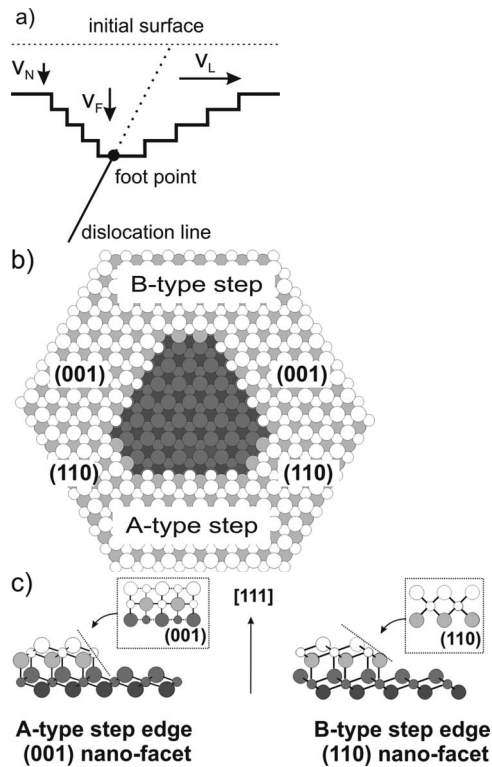


FIG. 2. (a) Schematic representation of the etch process at a dislocation line with inclination to the surface plane. The etch pit deepens with the frontal etch velocity  $v_F$  and steps move laterally with the velocity  $v_L$ . The inclination of the dislocation line yields etch pit walls with different inclinations and consequently different step densities. Independent of the presence of the dislocation, the surface is etched with a velocity  $v_N$ . As  $v_F$  and  $v_L$  are larger than  $v_N$ , the etch pit enlarges in all dimensions as a function of etching time. (b) Top view on the CaF<sub>2</sub> (111) surface with a flat pit to illustrate the difference between A-type and B-type steps. The brighter circles describe the upper layer and the darker circles describe the lower layer. (c) Side view of fluorite step structures in the [110] direction. Small circles denote calcium ions and big circles represent fluoride ions. The A-type steps are (001) facets enclosing an angle of 54.74° with the (111) surface and B-type steps are (110) facets enclosing an angle of 70.53° with the (111) surface.

will refer to them as double pointed etch pits. They are the result of complex subsurface defect structures and will be discussed in the context of an arrangement of etch pits in Sec. III C. For all applied etches and etching conditions, we find the two categories of etch pits introduced in Fig. 1(b), namely, pointed etch pits and flat bottom etch pits and propose that their morphological characteristics are related to the structure of subsurface defects as will be discussed in detail below.

The process of etching the surface at significant undersaturation can be described by three processes sketched in Fig. 2(a). First, the flat perfect surface retreats by a process commonly referred to as spontaneous hole nucleation at the speed  $v_N$ . Hole nucleation is the irreversible removal of crystal units from the surface forming a monolayer-deep pit that is constantly enlarged as a function of time. At the atomic scale, the number of bonds between crystal units determines the dissolution probability explaining why kink positions are removed faster than step edges or units from a complete surface layer. As a result, during etching every cleavage step is displaced and often attains a curvature. In addition to already existing cleavage steps, steps are formed on the surface by the formation and deepening of etch pits.

Second, the macroscopic etch pit formation at dislocation defects occurs via enhanced two-dimensional hole nucleation at and close to the dislocation emergence point. The removal of crystal units is accelerated by the stress field caused by the dislocation. The etch pit deepens at the speed  $v_F$  and follows the dislocation line which makes the etch pit eccentric. Third, one observes the lateral displacement of steps away from the dislocation source at the speed  $v_L$ . The macroscopic shape of the resulting step train moving away from the dislocation emergence point determines the appearance of the confining walls of the respective etch pit. During the evolution of the etch pit, the time-dependent adsorption and desorption of reaction products or impurities may alter the profile of the step train according to Frank's kinematic wave theory of dissolution.<sup>11,23</sup>

The crystallographic orientation of the etch pit borders is determined by the crystal lattice structure and commonly understood in terms of periodic bond chain vectors defined by the direction of the strongest bonds. The strongest binding force between neighboring ions on the (111) surface is along the [110] direction.<sup>24</sup> Therefore, the separation of those neighbors is less likely to happen and steps of this orientation remain as the most stable.

Due to the  $c_3$  symmetry of the (111) surface, etch pits normally appear with threefold symmetry having their confining outer edges in the [110] equivalent directions.<sup>25</sup> As illustrated in the atomic structure models of Figs. 2(b) and 2(c), there are two kinds of step edges in the [110] direction on the (111) surface of a fcc crystal, namely, (001) nanofaceted steps (A type) and (110) nanofaceted steps (B type).<sup>26</sup>

Usually the B-type steps do not appear in etch figures as they are less stable than A-type steps. Therefore, most etch pits have a triangular shape; however, under certain circumstances B-type steps appear and result in the formation of ditrigonal etch pits.

A flat bottom in an etch pits occurs when the origin of the enhanced stress is no longer active and the dissolution speed of crystal surface and etch pit bottom proceed at the same speed. Flat pits have so far not been included in investigating the etched crystals since their detection and investigation is intricate; however, SFM can access these etch figures and provide insight into near-surface defect structures.

## B. Comparison of etch media

We etch freshly cleaved (111) fluorite plates using nitric acid, hydrochloric acid, sulfuric acid, and orthophosphoric acid at different concentrations and chose temperature and etch duration to obtain mainly etch pits which are clearly distinguishable as single features. Here we describe and discuss the morphological appearance caused by the different etch media and later kinetics and specific effects.

An overview of the CaF<sub>2</sub> (111) etch figures is given in Fig. 3 whereby each row presents results from one acid in the sequence from top to bottom of HNO<sub>3</sub>, HCl, H<sub>2</sub>SO<sub>4</sub>, and H<sub>3</sub>PO<sub>4</sub>. The typical dislocation etch pit created by concentrated nitric acid ( $w=65\%$  and  $c=15.8$  mol/l) shown in frame (a) is trigonal and has terraced walls. The marginal edges appear erratic and the terracing of the inner walls gives

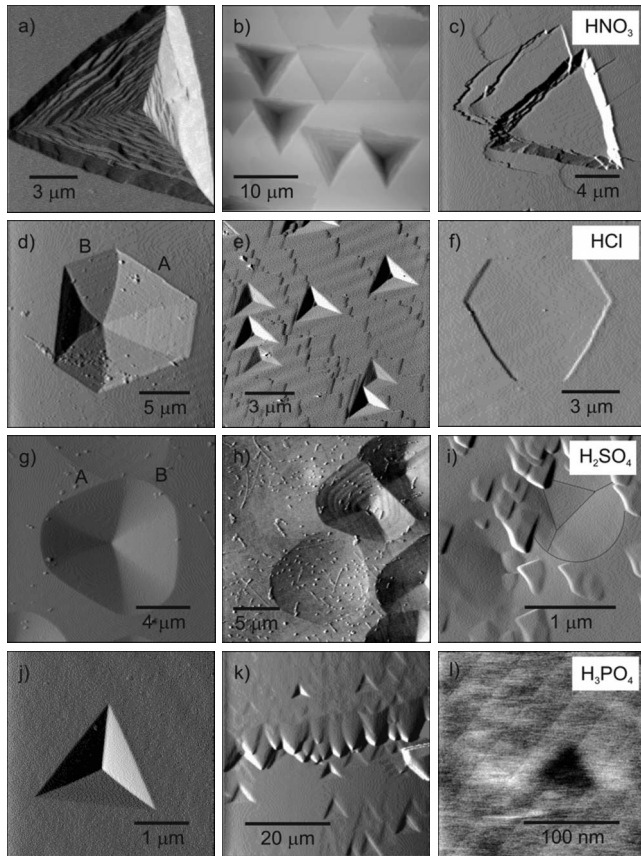


FIG. 3. Etch pits and cleavage steps after treatment with various acids. (a)–(c) Etching with concentrated  $\text{HNO}_3$ . (a) Pointed etch pit with an edge length of  $14 \mu\text{m}$  and a depth of  $1.4 \mu\text{m}$  (30 min at 296 K). (b) Four neighboring terraced pointed etch pits having different eccentricities (5 min at 313 K; side lengths are  $10.2 \mu\text{m}$ , depths of pits from left to right are 772, 803, 515, and 934 nm). (c) Flat pit with typical erratic edges ( $11.3 \mu\text{m}$  side length and 311 nm depth) superimposed by a less deep second one (5 min at 313 K). (d)–(f) Etching with HCl. (d) Ditrigrone etch pit produced by high acid concentration exhibiting A-type steps alternating with B-type steps (12.4 M, 10 min at 298 K). The protrusions in the interior of the pit result from a trial postetching treatment. (e) Etching at low concentration produces triangular etch pits (2 M, 9 min at 296 K). (f) Ditrigrone flat pit produced by etching at high concentration (12.6 M, 5 min at 298 K). (g)–(i) Etching with  $\text{H}_2\text{SO}_4$ . (g) and (h) exhibit ditrigrone etch pits of  $10 \mu\text{m}$  widths and up to 800 nm depth (18 M, 5 min at 297 K). (h) The protrusions in this frame were not present in the first scan of this area but were the result of tip-induced precipitation. (i) Ditrigrone flat pit with a trigonal plateau having a depth of 61 nm (7 M, 5 min at 302 K; borders are highlighted). The protrusions partly covering the etch pit were formed during etching and have a height of up to 50 nm. (j)–(l) Etching with concentrated  $\text{H}_3\text{PO}_4$ . (j) Etch pit with  $2.2 \mu\text{m}$  side length and 110 nm depth (30 min at 345 K). (k) A zigzag-shaped cleavage step appears smoothed after etching (15 min at 378 K). (l) Very small flat pit with a side length of 70 nm and a depth of 1.5 nm, corresponding to the height of five F-Ca-F triple layers (30 min at 335 K).

the etch pit a scalelike structure with step terraces that are irregular but parallel to the surface. Frame (b) shows a topographic image exhibiting a group of etch pits having different depths where strongly eccentric etch pits are shallower than less eccentric ones. Flat pits having erratic step edges [frame (c)] appear with a morphology similar to that of pointed etch pits.

Hydrochloric acid was applied at high [12.4 M, frames (d) and (f)] and low [2 M, frame (e)] concentrations. At high concentration and sufficient etching time, we observe ditrigrone etch pits having straight B-type step edges (d). The

TABLE I. Comparison of the applied acid etch speeds and reaction products solubility. Frontal and lateral etch speeds at 296 K etch temperature for different etchants related to the solubility of their reaction products (concentration of  $\text{Ca}^{2+}$  in saturated solution calculated from Ref. 39). For comparison, the  $\text{CaF}_2$  solubility in water is 0.0002 mol/l.

Acid	Frontal etch speed $v_F$ (nm/min)	Lateral etch speed $v_L$ (nm/min)	Reaction product	Solubility of reaction product (mol/l)
$\text{HNO}_3$	46	200	$\text{Ca}(\text{NO}_3)_2$	8.7
HCl (2 M)	13	140	$\text{CaCl}_2$	7.3
HCl (12.4 M)	54	680	$\text{CaCl}_2$	7.3
$\text{H}_2\text{SO}_4$	140	910	$\text{CaSO}_4$	0.015
$\text{H}_3\text{PO}_4$	0.12	10	$\text{Ca}_3(\text{PO}_4)_2$	0.000012

etchings by 2 M HCl occur slower and etch pits do not appear ditrigrone. Etching with HCl in concentrations leading to ditrigrone pointed etch pits also yields flat pits containing B-type steps [frame (f)].

Etching with concentrated sulfuric acid (18 M) also results in ditrigrone pits [frames (g) and (h)]. In contrast to the results obtained using concentrated hydrochloric acid, B-type steps are slightly curved away from the center [frame (g)]. The treatment with concentrated  $\text{H}_2\text{SO}_4$  results in lens-shaped rounded smooth ditrigrone flat pits [frame (h)]. Frame (i) that is the result of etching by 7 M  $\text{H}_2\text{SO}_4$  shows a rare flat pit with inner edges forming a distinct trigonal plateau on its bottom and a smooth curvature on its outer region. The protrusions on frame (h) appeared after repeated scanning whereas the protrusions on frame (i) can be seen right after the first scan.

Distinguished trigonal etch pits with very smooth faces [frames (j) and (k)] are obtained with concentrated  $\text{H}_3\text{PO}_4$  ( $w=85\%$  and  $c=14.83 \text{ mol/l}$ ). Frame (k) shows an etched cleavage step with a zigzag pattern. Very small etch pits [frame (l)] can be created reproducibly and controllably facilitating the study of areas with a high dislocation density as they occur in the vicinity of grain boundaries.

### C. Dissolution kinetics

As apparent from images compiled in Fig. 3, we can create a variety of very different morphologies when etching the same surface with different acids. To understand the observed phenomena, we have to identify the dissolution mechanism and the related dissolution kinetics for the different acids. The etching process comprises several steps, namely, the reaction of surface crystal units with the medium, the successive diffusion on the surface, detachment from the surface, and diffusion into the solution volume. To define the mechanism, the main question to be clarified is whether the process is controlled by the diffusion rate or by the reaction rate which depends on the details of detachment of crystal units from the surface. The speed can be determined solely by the diffusion process from the surface into the solution or solely by the surface reaction. The kinetic limitation of the reaction speed is determined by the slowest step of the entire dissolution process.<sup>27</sup>

In Table I we compile data for etch pit frontal and lateral speed for the different acids. Since we used no stirring in our

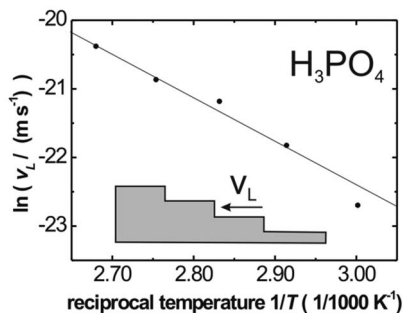


FIG. 4. Arrhenius plot of the lateral dissolution speed  $v_L$  for an etch with concentrated phosphoric acid. From the Arrhenius equation  $v_L = A \exp(-E_A/kT)$  we deduce an activation energy of  $E_A = 0.60$  eV, where  $A$  is a prefactor,  $k$  is the Boltzmann constant, and  $T$  is the etchant temperature in Kelvin.

vessel, the hydrodynamic condition is sensitive to slightest disturbances and, therefore, these compiled numbers are only our observed maxima but they may vary over the surface of a given crystal. Therefore, some surface regions may exhibit a decreased dissolution speed and consequently exhibit smaller etch pits.

At room temperature, the etching speed is largest for sulfuric acid, then nitric acid, and hydrochloric acid and etching occurs comparatively slowly for phosphoric acid. For the same acid, the dissolution speed scales with the hydrogen concentration as seen for HCl where the etch proceeds roughly 5 times faster for the 12.4 M than for the 2 M acid. This is generally true for the same acid as long as the same mechanism is effective at different concentrations. For the same acid and the same dissolution mechanism, lower pH values result in a faster dissolution since the protons adsorbed at the surface lead to a higher surface charge on the crystal accelerating the dissolution.<sup>28</sup>

The activation energy for the etch process relates the kinetic behavior to the temperature. Nicoara *et al.*<sup>19</sup> analyzed dissolution of fluorite by hydrochloric acid using an Arrhenius analysis to determine the activation energy for lateral dissolution. In such an analysis, activation energies larger than 0.5 eV are empirically attributed to a reaction-rate-controlled process. For hydrochloric acid they found an activation energy of 0.35–0.75 eV depending on the etchant concentration. Desai and John<sup>21</sup> investigated the activation energy for sulfuric acid and found activation energies of 0.49–0.82 eV. We determined the activation energy for phosphoric acid and deduce from the Arrhenius plot shown in Fig. 4 an activation energy of  $0.60 \pm 0.08$  eV suggesting a reaction-rate-controlled formation of dislocation etch pits.

The mechanism active for  $\text{H}_3\text{PO}_4$  is reaction-rate-controlled due to the high activation energy similar to the case of  $\text{H}_2\text{SO}_4$ . The less reaction-controlled dissolution kinetics governing etching by  $\text{HNO}_3$  or HCl is more sensitive to hydrodynamic disturbances and geometric conditions since the diffusion can easily be affected by such parameters. Phosphoric acid provides some advantage since etching occurs rather slowly and controlled.

A reaction-rate-controlled dissolution implies that the behavior of the formed reaction product determines the entire process as a kinetic bottleneck. The comparison of the

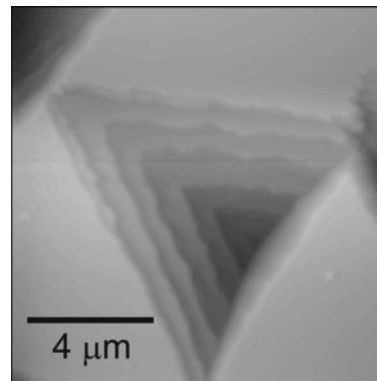


FIG. 5. Enlarged view of the third (from left to right) etch pit taken from Fig. 3(b). This etch pit is 530 nm deep and exhibits a strong eccentricity. The two shallow walls have a distinct terrace structure with ledge widths of 0.2–0.4  $\mu\text{m}$  and a step height of 50–200 nm. The third face is much steeper and exhibits a rather smooth surface composed of much smaller steps.

solubility of the reaction products by all acids with fluorite indicates the trend between dominantly reaction-rate-controlled dissolution and sparingly soluble reaction products. With orthophosphoric acid, the reaction product is less soluble than  $\text{CaF}_2$  itself (see Table I) and the reaction is rate controlled increasing the reproducibility<sup>29</sup> of distinct dislocation etch pit features because the dissolution process is not strongly influenced by diffusion.

## D. Etching phenomena

### 1. Terracing of etch pit walls

The profile of the step arrangement in an etch pit wall is commonly referred to as a step train and if the interspacing is regular the etch pit walls appear macroscopically smooth. However, the etch pit walls caused by nitric acid bear a conspicuously terraced character as seen in Figs. 1(b), 3(a), and 3(b) and the detail image shown in Fig. 5. A similar phenomenon has been observed by Desai *et al.* reporting the formation of step ledges when etching with hydrochloric acid vapor<sup>30</sup> while we observe that etching by concentrated hydrochloric acid does not produce terrace patterns.

Terracing results from step bunching which is the convergence of several steps into a single step of multiple height. In the kinematic wave theory, this is explained by the diffusion of adatoms over steps in the step train. Time-dependent adsorption/desorption<sup>31</sup> of diffusing adatoms on the terraces can lead to perturbations in the diffusion field which may yield the formation of step bunches during the etching process.<sup>32</sup> The attachment or detachment of adatoms thereby influences the movement of single steps and, hence, also the terracing character of etch pit walls. Adatoms different from pristine crystal units are called poisons and originate from reaction products of detached crystal units. According to Frank's kinematic theory, step bunching is more likely to occur at high reactant concentrations and low dwell times of poisons on the ledges. This is the case for nitric acid where the dissolution proceeds at high rates and the highly soluble reaction product (see Table I) does not remain on etch pit terraces for a long time. In contrast, the reaction products from sulfuric acid and phosphoric acid are much

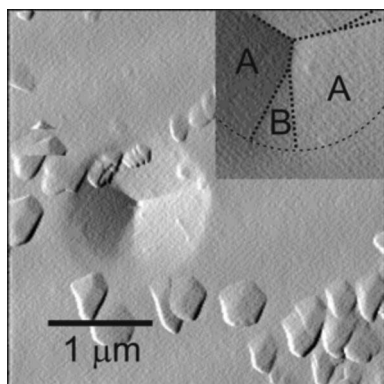


FIG. 6. This pointed etch pit represents a transition morphology between trigonal symmetry in the inner and ditrigonal symmetry in the outer areas (7 M sulfuric acid, 5 min at 302 K). The center of the etch pit is displayed in the magnified image in the upper right corner where borders between regions of A-type steps and B-type steps are highlighted. During the etching process protrusions are grown and partially cover the etch pit and the surrounding surface regions.

less soluble (see Table I) and, hence, their dwell time on the ledges will be longer preserving the step train and hindering the formation of step bunches.

Figure 3(b) shows four eccentric pits resulting from nitric acid etching. The ledges of the terraces have irregular borders and the height of walls separating terraces differ from each other. A magnification of one of the etch pits shown in Fig. 5 reveals that the three confining walls of the eccentric etch pit have different slopes. The steepest wall is substantially smoother than the others due to a higher step density and shorter step interspacings, an observation that becomes immediately evident from the sketch shown in Fig. 2(a). A shorter step interspacing implies that the resulting diffusion field determining the respective ledge is less susceptible to being disturbed while etching. Therefore, step bunching is less likely to occur at high step densities of walls leading to the fact that the steepest wall in an eccentric etch pit remains the smoothest during prolonged etching.

Interstep interactions leading to bunch formations are complex to formalize; however, SFM is capable of investigating the detailed pattern formation on stepped surfaces and can, therefore, contribute to the understanding of interstep interactions.<sup>33</sup> A strength of the technique in this context is that with SFM we cannot only explore etch pit shapes and step morphology but can also measure step heights and step details with highest precision.

### E. Ditrigonal etch pits

Usually the observed etch pits have three confining walls but certain conditions can result in the formation of ditrigonal etch pits [Figs. 3(d) and 3(g)]. At the beginning of the etching process, always trigonal etch pits are formed that are solely composed of A-type step edges. However, prolonged etching by concentrated hydrochloric acid or sulfuric acid causes the appearance of B-type steps between the A-type steps [Figs. 3(d) and 3(g)]. In Fig. 6 we grasp a situation illustrating the transition from a trigonal to a ditrigonal etch pit. There we find that in the center solely A-type steps appear while B-type steps develop at some height and form

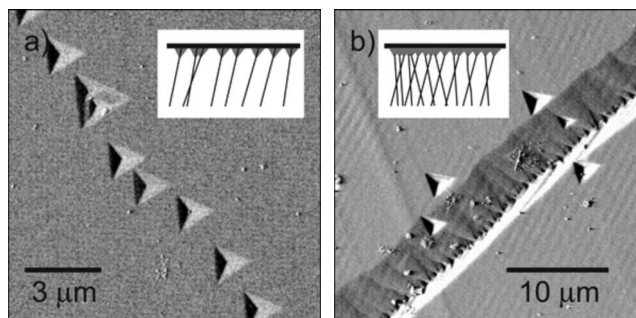


FIG. 7. Trains of pointed etch pits related to hidden crystal boundaries with different dislocation network compositions. The schemes in the images are schematic sketches of the anticipated dislocation structures. (a) The crystal boundary leaves a row of single etch pits having interspacings that are roughly regular. The second etch pit from the left could be due to a dislocation junction (2.3 M HCl, 2 min at 294 K). (b) Crystal boundary appearing as a trench decorated with miniature etch pits in the bottom middle line (concentrated  $\text{H}_3\text{PO}_4$ , 60 min at 333 K). Such trenches are associated with a very high density of dislocations frequently crossing each other.

wedge-shaped areas that can be expected to develop into circular sectors during further etching. For geometric reasons, B-type steps have a higher reactivity than A-type steps and they can only exist due to the movement of step edges. The relative speed of two processes are relevant for the movement of steps according to the Burton, Cabrera, and Frank theory of crystal growth.<sup>34</sup> One is the formation of double kinks in a step edge when a single unit is removed from a straight edge. The other is the successive removal of kink atoms until the kink positions reach the end of a step. In etch pits having only A-type steps, the rate of removing single kink positions is much higher than double kink formation and, therefore, the kink position travels to the end of an edge, and as a result the step edge remains straight and smooth. Further growth of the etch pit leads to longer step edge lengths and the formation of double kinks may take place in a step edge before the preceding (single) kinks have reached the end of the respective step edge. So the remaining kink positions of the step edge add up and constitute B-type steps at the ends of the A-type steps. In this case, the appearance of B-type steps depends on the difference between the double kink formation rate and the successive kink removal rate. B-type step occurrence is more likely if either double kink formation is enhanced or the removal of single kink positions is impeded. Due to the high activity of concentrated HCl, double kink formation is enhanced in relation to kink position removal and causes the occurrence of ditrigonal etch pits. Sulfuric acid, on the other hand, has a reduced single kink removal rate due to the sparingly soluble reaction product limiting the step edge enlargement and remaining single kinks form the B-type steps. Hence, we attribute the qualitative differences of straight steps for HCl [Fig. 3(d)] and outward curved B-type steps for  $\text{H}_2\text{SO}_4$  [Fig. 3(g)] to the low solubility of the reaction product calcium sulfate compared to the good solubility of calcium chloride.

### F. Arrangements of etch pits

When appearing with high density, dislocations are often interlinked or looped and form networks. Cleavage may pro-

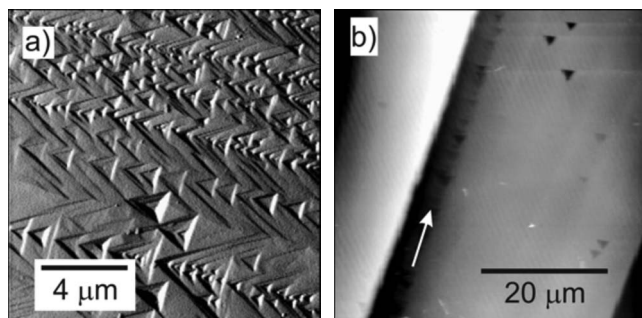


FIG. 8. (a) Demonstration of the movement of etch pits resulting from dislocations induced by stress applied with the tip of a tweezers to the surface (concentrated  $\text{H}_3\text{PO}_4$ , 10 min at 365 K). Etching immediately after this treatment displays tracks of apparent flat pits. The applied stress source is some distance away from this imaged position, so that the mobile dislocations appear as parallel tracks. Some dislocations passed later in the same track and left smaller tracks of etch pits within the tracks. (b) Train of flat pits aligned along a cleavage step. Such trains next to steps are often found in a situation of nonperfect cleavage. This example shows a cleavage step of 136 nm height accompanied by a series of flat pits of up to 12 nm depth (concentrated  $\text{H}_3\text{PO}_4$ , 35 min at 341 K).

duce cuts throughout such three-dimensional dislocation structures and, therefore, after etching pits frequently appear in conspicuous arrangements as demonstrated in the examples compiled in Fig. 7. Crystal boundaries such as grain boundaries that are formed by dislocation networks appear on the surface after etching as linear rows of pointed etch pits.<sup>35</sup> These linear arrangements may appear as a sequence of single etch pits [Fig. 7(a)] or, at a high density of dislocations, the etch figures coalesce into a trench as seen in Fig. 7(b).

Within sequences of separated etch pits there are sometimes double pointed etch pits like the second one from the left in Fig. 7(a). This pit is characterized by two neighboring smaller eccentric etch pits on the bottom which have a different edge length. While the length of edge borders of single pointed etch pits within such sequences are roughly the same, the double pointed etch pits have significantly longer borders. Since the vertical dissolution speed  $v_L$  is the same for all steps, the double pointed pit cannot originate from a single dislocation line and we speculate that the double pointed etch pit is due to etching of intersecting dislocation lines. Within this interpretation, the two small etch pits within the pit are the result of branching in the underlying dislocation structure. This interpretation is supported by the observation that the flat bottom areas in this big etch pit are not parallel to the outer surface which distinguishes them from simple flat bottomed etch pits. Intersections of dislocation lines may lead to the formation of dislocation nodes, a phenomenon that is well described in the context of work hardening of metals.<sup>36</sup>

The formation of linear rows of flat pits can be studied by locally applying force prior to etching as demonstrated by the dense pattern of dislocation traces shown in Fig. 8(a). This pattern is the result of stress produced by pressing the tip of tweezers onto the surface causing dislocations that are not fixated but move away from the stress source through the crystal. Such a movement occurs in a series of jumps rather than a continuous movement.<sup>37</sup> If the etching occurs while

the dislocations are moving, the surface reveals their movements as tracks of flat pits. During the dwell time on a site, an etch pit is formed and then evolves as a flat pit after the dislocation line hopped to the next location. The flat pits within a track have roughly the same distance to their neighbor suggesting a constant velocity for the movement of dislocations.

In a number of cases, we also found an increased flat pit population next to cleavage steps as demonstrated in Fig. 8(b). These flat pits are aligned along the cleavage step, follow its curvature, and appear always on the lower terrace next to the cleavage step. However, there is no regular distance between these flat pits and they have slightly different depths. Therefore, it is unlikely that they are the result of moving dislocations. We anticipate that such patterns are caused by the cleavage process since we find more cleavage steps combined with flat pit arrangements on samples that did not cleave perfectly.

### G. Spontaneous and scanning induced growth of precipitates

It has been reported in literature that sulfuric acid as etchant may cause the growth of protruding  $\text{CaSO}_4$  structures on the fluorite surface during the etching process.<sup>20</sup> The typical appearance of such structures appearing in our experiments when etching with 7 M  $\text{H}_2\text{SO}_4$  can be seen in Figs. 3(i) and 6. They evolve during etching and may cover etch pits and this may deteriorate a detailed analysis of the size and shape of etch figures.

On the contrary, surfaces freshly etched with 14 M  $\text{H}_2\text{SO}_4$  and scanned with the SFM for the first time appear to be almost free from any protruding features [Fig. 3(g)] while successive imaging of the same area yields numerous precipitates [Fig. 3(h)]. This phenomenon is also observed for etching with  $\text{H}_3\text{PO}_4$  as clearly seen by the successively recorded images shown in Figs. 9(a) and 9(b). Further imaging of the same area yields precipitates growing in size and number. It is clear that a quantitative SFM analysis of etching figures is massively hampered by the growth of such scanning induced surface structures. This phenomenon is similar to findings reported by Finot *et al.*<sup>38</sup> who observed a precipitationlike process on gypsum ( $\text{CaSO}_4 \cdot 2\text{H}_2\text{O}$ ) surfaces induced by the scanning tip of an SFM. The occurrence of precipitation was found to be very sensitive to the relative humidity of the air present while scanning and we conclude that the water meniscus in association with the force field between tip and surface supports the relocation of material during scanning. A similar process might be active in our case whereby the force field of the SFM tip causes the detachment of adsorbed anions from the etchant and nucleation and growth in form of the observed protrusions. Coverage of the surface with anions is expected for etchants producing reaction products with low solubility and this explains why the phenomenon of tip induced growth of protrusions is primarily observed for  $\text{H}_2\text{SO}_4$  and  $\text{H}_3\text{PO}_4$  (see Table I). The proposed mechanism of tip induced precipitation is illustrated in Fig. 9(c). After etching and drying, the fluorite crystal is covered by an amorphous layer of hardly soluble reac-

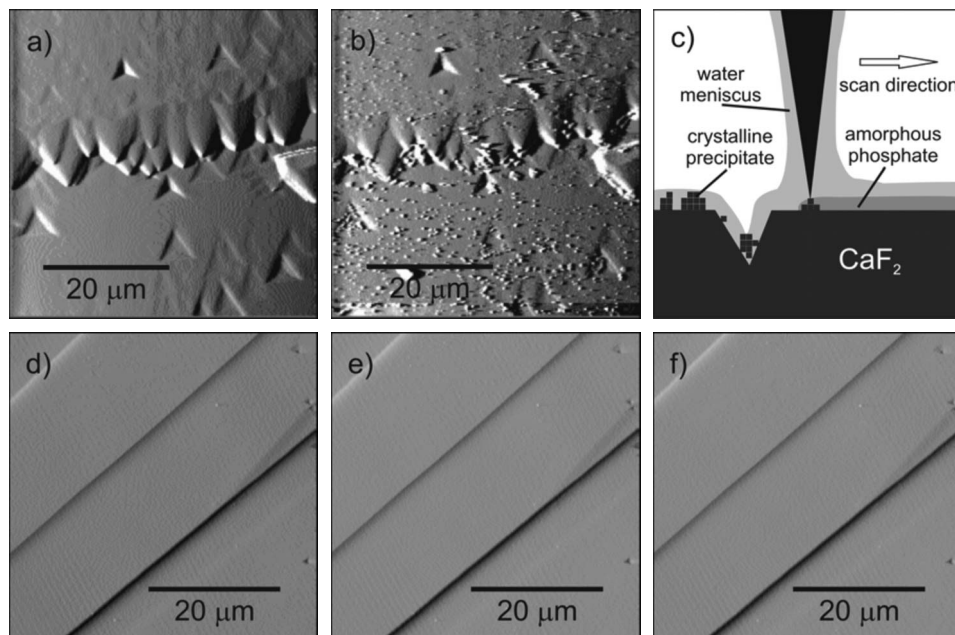


FIG. 9. (a)–(c) Demonstration of SFM scanning induced precipitation after etching with concentrated  $\text{H}_3\text{PO}_4$ . (a) Protrusion free surface after the first scan (15 min at 378 K). (b) A large number of precipitates is found in the second scan taken 15 min after the first one and all following scans (not shown). (c) Scheme illustrating the process of scanning induced precipitation. The process is facilitated by the force field between tip and surface present during scanning. Within the water film on the surface and the water meniscus surrounding the tip, the homogeneous film of adsorbed phosphate is dissolved and crystalline calcium phosphate is formed by the action of the tip. (d)–(f) Demonstration of the success of postetching treatment by  $\text{HNO}_3$  and rinsing with water to keep the surface free of precipitates. (concentrated  $\text{H}_3\text{PO}_4$ , 15 min at 355 K). (d) The first scan exhibits a perfectly clean surface. (e) Images of the following scan (taken 20 min after the first one) and (f) a third scan (taken 2 h after the first one) do not exhibit any precipitates.

tion products homogeneously spread over the surface that appears to be smooth. This layer is partially dissolved in the water film on the surface that is always present when exposing the surface to air. The material from the amorphous layer is transformed into calcium sulfate or calcium phosphate crystals in the force field of the scanning tip. The scanning tip leaves behind an area with randomly nucleated crystallites that grow in number during repetitive scanning until the material from the amorphous layer is used up.

For a quantitative analysis of etch figures with the SFM, precipitates are most hindering and, therefore, we were seeking for a strategy to avoid surface precipitation. We tried to remove precipitates by washing the freshly etched crystal in a neutralization bath (sodium hydroxide solution at pH  $\sim 7$ –8); however, this would not yield the desired result. Also prolonged washing in distilled water and heavy stirring during etching and washing do not stop the growth of protrusions.

For the case of phosphoric acid, we can eliminate or at least strongly reduce scanning induced precipitation by a special post etching treatment including a short etch with nitric acid. The success of this strategy is documented in the series of images compiled in Figs. 9(d)–9(f). These three frames represent images taken immediately after the postetching procedure [frame (d)], with the same area imaged 20 min later [frame (e)] and 120 min later [frame (f)]. Scanning results are identical and not a single precipitate can be detected on the surface. As a simple explanation for this result we propose that the solubility of the reaction product formed when etching with nitric acid is much higher than that of etching with phosphoric or sulfuric acid (see Table I).

Hence, dipping the etched surface in diluted nitric acid dissolves the amorphous layer left from etching with phosphoric acid and the soluble reaction products are washed away by the subsequent rinsing in the neutralization bath. In many similar experiments, we verified that the described postetching treatment yields etched surfaces that are clean and stable over months of observation facilitating a detailed and repetitive SFM inspection of etching figures. Therefore, we adopted this procedure for all measurements except the initial demonstration experiments shown in Figs. 3, 6, and 9.

#### IV. SUMMARY

We introduce SFM as a versatile method for high resolution studies of etch figures. This approach provides direct access to microscale and nanoscale topographic features of etched cleavage plates and allows a quantitative analysis and detailed understanding of etch figures. Due to the high resolution of the SFM, smallest features and areas containing a high density of etch pits are accessible for a detailed inspection. Both, qualitative and quantitative knowledge of the dislocation etch pit characteristics such as pointed etch pits versus flat bottom pits, eccentricity, terracing, and ditrigonal shapes provide most valuable information for the identification of characteristic morphologies and for the definition of categories describing certain etching phenomena. Besides a detailed analysis of pointed etch pits that are related to dislocations, SFM allows the detection and characterization of flat pit structures that are associated with crystal defects such

as voids and impurity aggregates. Rows of flat pits next to cleavage steps are associated with peculiarities of the cleavage process.

The quantitative analysis of etch pits facilitates an identification of the kinetic characteristics of the etching process. The morphology of the etch pits and the structure of etched cleavage steps are characteristic features of the respective etch medium. At room temperature, etching proceeds very quickly with  $\text{HNO}_3$ ,  $\text{HCl}$ , and  $\text{H}_2\text{SO}_4$  which leads to the merging of etch pits at areas of high dislocation densities, whereas etching with  $\text{H}_3\text{PO}_4$  proceeds much slower and the process is much easier to control. The solubility of the reaction products is found to be the key to the dissolution kinetics and, hence, determines the morphology of the dislocation etch pits and other etching features. For the lateral dissolution by phosphoric acid, we find an activation energy of 0.60 eV pointing to a reaction-rate-controlled process. Due to this kinetic characteristics and the small etching speed, phosphoric acid is best suited for obtaining well defined small etch pits. Another advantage of etching with phosphoric acid is that it produces pits that are solely trigonal and have well defined edges in contrast to the more fuzzy shape of steps and step bunching structures found for other etchants such as  $\text{HNO}_3$ . The problem of scanning induced precipitates present for etching with sulfuric and phosphoric acids can be solved by an appropriate post-etching procedure. In summary, phosphoric acid is the best choice for a controlled production of scalable etching figures on  $\text{CaF}_2$  (111) that are well accessible for a quantitative characterization by SFM imaging.

- <sup>1</sup>K. A. Bates, M. Rothschild, T. M. Bloomstein, T. H. Fedynyshyn, R. R. Kunz, V. Liberman, and M. Switkes, *IBM J. Res. Develop.* **45**, 605 (2001).  
<sup>2</sup>M. Rothschild, T. M. Bloomstein, J. E. Curtin, D. K. Downs, T. H. Fedynyshyn, D. E. Hardy, R. R. Kunz, V. Liberman, J. H. C. Sedlacek, R. S. Uttaro, A. K. Bates, and C. Van Peski, *J. Vac. Sci. Technol. B* **17**, 3262 (1999).  
<sup>3</sup>J. Sils, M. Reichling, E. Matthias, and H. Johansen, *Czech. J. Phys.* **49**, 1737 (1999).  
<sup>4</sup>T. Westerhoff, K. Knapp, and E. Moersen, *Proc. SPIE-Int. Soc. Opt. Eng.* **3424**, 10 (1998).  
<sup>5</sup>J. Staebelin, A. Weisleder, G. Wehrhan, B. Speit, and L. Parthier, (unpublished).  
<sup>6</sup>J. H. Burnett, Z. H. Levine, and E. L. Shirley, *Phys. Rev. B* **64**, 241102 (2001).

- <sup>7</sup>C. Görling, U. Leinhos, and K. Mann, *Opt. Commun.* **249**, 319 (2005).  
<sup>8</sup>R. P. Vaudo, X. Xu, C. Loria, A. D. Salant, J. S. Flynn, and G. R. Brandes, *Phys. Status Solidi C* **0**, 494 (2002).  
<sup>9</sup>B. Cockayne and D. S. Robertson, *Nature (London)* **203**, 1376 (1964).  
<sup>10</sup>W. Kleber, M. Hahnert, and I. Lüdtke, *Krist. Tech.* **1**, 585 (1966).  
<sup>11</sup>K. Sangwal, *Etching of Crystals: Theory, Experiment and Application*, Defects in Solids Vol. 15 (Elsevier, Amsterdam, 1987).  
<sup>12</sup>R. B. Heimann, *Auflösung von Kristallen: Theorie und Technische Anwendung* (Springer, Wien, NY, 1975).  
<sup>13</sup>H. H. Teng and P. M. Dove, *Am. Mineral.* **82**, 878 (1997).  
<sup>14</sup>R. S. Arvidson, M. Collier, K. J. Davis, M. D. Vinson, J. E. Amonette, and A. Luttge, *Geochim. Cosmochim. Acta* **70**, 583 (2006).  
<sup>15</sup>G. Jordan and W. Rammensee, *Surf. Sci.* **371**, 371 (1997).  
<sup>16</sup>R. S. Retherford, R. Sabia, and V. P. Sokira, *Appl. Surf. Sci.* **183**, 264 (2001).  
<sup>17</sup>S. Gritschneider, Y. Namba, and M. Reichling, *Nanotechnology* **16**, 883 (2005).  
<sup>18</sup>C. C. Desai, *Cryst. Res. Technol.* **16**, 437 (1981).  
<sup>19</sup>I. Nicoară, O. F. G. Aczel, D. Nicoară, and Z. Schlett, *Cryst. Res. Technol.* **21**, 647 (1986).  
<sup>20</sup>K. Sangwal, C. C. Desai, and V. John, *Krist. Tech.* **14**, 63 (1979).  
<sup>21</sup>C. C. Desai and V. John, *Krist. Tech.* **14**, 295 (1979).  
<sup>22</sup>J. B. Engelhardt, H. Dabringhaus, and K. Wandelt, *Surf. Sci.* **448**, 187 (2000).  
<sup>23</sup>F. C. Frank, in *Growth Perfection Crystals*, edited by R. H. Doremus, B. W. Roberts, and D. Turnbull (Wiley, New York, 1958), pp. 411–419.  
<sup>24</sup>P. Hartman, *Neues Jahrb. Mineral., Monatsh.* **1959**, 73.  
<sup>25</sup>G. Tammann and W. Krings, *Z. Anorg. Allg. Chem.* **146**, 420 (1925).  
<sup>26</sup>V. E. Puchin, A. V. Puchina, M. Huisinga, and M. Reichling, *J. Phys.: Condens. Matter* **13**, 2081 (2001).  
<sup>27</sup>S. S. Zumdahl, *Chemical Principles*, 5th ed. (Houghton, Boston, 2005), pp. 727–728.  
<sup>28</sup>W. Stumm, *Colloids Surf. A* **120**, 143 (1997).  
<sup>29</sup>J. V. Macpherson and P. R. Unwin, *Prog. React. Kinet.* **20**, 185 (1995).  
<sup>30</sup>C. C. Desai, K. Sangwal, and V. John, *Krist. Tech.* **12**, 1269 (1977).  
<sup>31</sup>M. B. Ives and J. P. Hirth, *J. Chem. Phys.* **33**, 517 (1960).  
<sup>32</sup>K. Sangwal, in *Etching of Crystals: Theory, Experiment and Application*, Defects in Solids Vol. 15 (Elsevier, Amsterdam, 1987), p. 290–292.  
<sup>33</sup>S. R. Coriell, A. A. Chernov, B. T. Murray, and G. B. McFadden, *J. Cryst. Growth* **183**, 669 (1998).  
<sup>34</sup>W. K. Burton, N. Cabrera, and E. C. Frank, *Philos. Trans. R. Soc. London, Ser. A* **243**, 299 (1951).  
<sup>35</sup>W. Bollmann, *Surf. Sci.* **31**, 1 (1972).  
<sup>36</sup>D. Hull and D. J. Bacon, *Introduction to Dislocations*, 4th ed. (Butterworth-Heinemann, Oxford, 2001).  
<sup>37</sup>W. G. Johnston and J. J. Gilman, *J. Appl. Phys.* **30**, 129 (1959).  
<sup>38</sup>E. Finot, E. Lesniewska, J. C. Mutin, and J. P. Goudonnet, *Surf. Sci.* **384**, 201 (1997).  
<sup>39</sup>D. R. Lide and H. P. R. Frederikse, *CRC Handbook of Chemistry and Physics*, 83rd ed. (CRC Press, Boca Raton, 2003).